The Astrophysical Journal, 738:152 (14pp), 2011 September 10 doi:10.1088/0004-637X/738/2/152

PRESTELLAR CORES IN THE COALSACK

M. Saul[1], M. Cunningham[1], J. Rathborne[2], W. Walsh[3], and H. M. Butner[4]
[1] School of Physics, University of New South Wales, Sydney, 2052 NSW, Australia; msaul@phys.unsw.edu.au, mariac@phys.unsw.edu.au
[2] Departamento de Astronomia, Las Condes, Santiago, Chile; rathborn@das.uchile.cl
[3] Harvard Smithsonian Center for Astrophysics, Cambridge, MA 02138, USA; wwalsh@cfa.harvard.edu
[4] Department of Physics and Astronomy, James Madison University, Harrisonburg, VA 22807, USA; butnerhm@jmu.edu
Received 2010 February 20; accepted 2011 April 13; published 2011 August 22

ABSTRACT

We present high spectral resolution millimeter mapped observations of seven prestellar cores in the Coalsack, including imaging in five optically thin molecular species of the kinematic structure of two of the densest cores, C2 and C4. Various collapse-critical indices are calculated; critical masses needed for collapse are consistently greater than those observed, the latter ranging from 0.4 to 2.4 $M_\odot$. The molecular emission in several of the cores shows line profiles with infall characteristics as well as elongated areas of increased line widths and reversals of center velocity gradients, implying that accretion disks may be forming.

Key words: ISM: clouds – ISM: molecules – ISM: structure – radio lines: ISM – stars: formation – stars: protostars

Online-only material: color figures

1. INTRODUCTION

Numerous searches for Population I objects in the Coalsack have been fruitless. Since the 1960s, unsuccessful searches have been conducted for H II regions (Hidajat 1962; Gómez & Mendoza v 1976; Le Coarer et al. 1992), flare, T Tauri, and OB stars (Weaver 1973; Muzzio & Orsatti 1977; Westerlund & Garnier 1989; Corradi & Franco 1995). Similarly, IR searches for young stellar objects (YSOs) have been in vain (Westerlund 1961; Jones et al. 1980, 1984; Smyth & Sim 1980), and no IRAS sources seem to be associated with the denser globules (Nyman et al. 1989; Kato et al. 1999). In contrast, other nearby cloud complexes such as the Auriga, Chamaeleon, Lupus, Ophiucus, and Taurus molecular clouds (e.g., Ungerechts & Thaddeus 1987; Wilking et al. 1989; Kenyon & Hartmann 1995) contain numerous YSOs. Although a wealth of literature attests to significant progress in recognizing physical conditions associated with protostars (e.g., see review by Evans 1999), limited high spectral resolution molecular mapping of prestellar regions in particular has precluded a detailed understanding of molecular cloud core formation, fragmentation, and collapse.

CO observations of the Coalsack were reported by Tapia (1973), Otrupcek & Wang (1987), and Vilas-Boas et al. (1994), who concentrated on the densest optical globules located near the cloud's western edge, site of the present study. Resolved formaldehyde and OH hyperfine components (Brooks et al. 1976) as well as CH radical Λ doubling structure (Andersson et al. 2002) and unprocessed ice mantles indicating very cool gas (Smith et al. 2002) are associated with these globules. Selected areas in the Coalsack have been the subject of color excess studies (Franco 1989; Naoi et al. 2007), showing evidence for a large abundance of silicates in C2, and Lada et al. (2004) identified an extinction minimum in C2 indicating the presence of a dense and pressurized circumnuclear ring of transient and possibly prestellar nature. Stellar extinction measurements identify a foreground and background cloud in addition to the main body of the Coalsack; the background cloud possibly corresponding to an H I shell arising as a windblown bubble from the CenOB1 association (McClure-Griffiths et al. 2001).

The seven cores observed here, C1–C7, were selected based on previous CO observations (see Table 1) identifying them as some of the densest regions in the Coalsack and possible sites of star formation (e.g., Figures 5, 7, and 9 in Nyman et al. 1989; Figures 2 and 5 in Kato et al. 1999). Recently, Rathborne et al. (2009) found C2 to be undergoing "outside-in" evolution amid a convergence of gas flows, consistent with ambipolar diffusion models (e.g., Shu & Li 1997) in which "inside–out" collapse as described by Shu et al. (1987) results only when a critical mass has diffused through the supporting magnetic fields. Here we extend the analysis into the optically thin regime (see Table 2 for molecules observed) in C2 and C4 and present CO, ^{13}CO, and C^{18}O results for all seven cores. First we describe the observations and key results, calculating various physical properties of the molecular cores; we then move to a discussion of three of the densest cores.

2. OBSERVATIONS

Observations with the 22 m Mopra antenna, near Coonabarabaran NSW, were made in the "on-the-fly" raster scanning mode, whereby each 5′.0 × 5′.0 field was mapped, the telescope continually scanning at a rate of 3″.5 s^{-1}, averaging data over a 2 s cycle interval, which gives an optimum data collection rate while not smearing output. Each Nyquist sampled map comprises at least 40 pixel rows and columns each, totalling 1600 spectra per field, except for the ^{12}CO, ^{13}CO, and C^{18}O lines in C2, which have 55 and 50, respectively, to encompass this core's larger emission area for which 14 maps were combined (seven R.A. (α), decl. (δ) scanned) to produce a ∼7′.0 × 7′.0 map of over 2500 usable spectra. The target fields were referenced to a fixed off (emission free) position for sky subtraction at α_{J2000} = 12 29 57.1, δ_{J2000} = −63 32 21.8.

The MOPS digital filterbank[5] was configured in narrowband "zoom" mode to provide 4096 channels, each 137.5 MHz wide, resulting in a velocity resolution at 115 GHz of ∼0.08 km s^{-1}. Each 8 GHz intermediate frequency (IF) is split into four 2.2 GHz bandwidth channels and down-converted to base band. The spectrometer produces four zoomed spectra for each IF, totalling 16 per configuration. Four zoom configurations were used from 85 to 115 GHz with the condition that the most

[5] http://www.narrabri.atnf.csiro.au/mopra/mops_techinfo.htm

Table 1
Observed Coalsack Cores

Core	Map Center $\alpha_{J2000}, \delta_{J2000}$	L_{12}[a] (pc)	L_{13}[b] (pc)	L_{18}[b] (pc)	A_{v13}[c] (mag)	A_{v18}[c] (mag)	Reference
C1	12 33 10, −63 42 01	0.11	0.20	0.10	2.9	5.3	∼Tapia 1[d]
C2	12 31 39, −63 44 58	0.20	0.31	0.23	3.0	6.9	∼K99 core 2[e]
C3	12 32 05, −63 49 30	0.10	0.20	0.11	2.3	4.8	∼N89 class A[f]
C4	12 30 19, −63 46 33	0.16	0.21	0.16	3.0	5.5	K99 core 1[e]
C5	12 33 00, −63 49 45	0.14	0.20	0.12	2.8	5.0	∼K99 core 3[e]
C6	12 33 58, −63 44 11	0.09	0.23	0.15	2.2	5.1	K99 core 4[e]
C7	12 33 50, −63 30 16	0.11	0.20	0.13	2.1	5.0	K99 core 5[e]

Notes. See Section 3.
[a] ^{12}CO geometric mean emission area diameter within 90% peak integrated intensity.
[b] ^{13}CO, C^{18}O $L = 2\sqrt{\frac{A}{\pi}}$, where A represents the area within half-peak integrated intensity.
[c] $\frac{N(\mathrm{H_2})}{A_v} = 9.4 \times 10^{20}$ (Savage & Mathis 1979).
[d] Tapia (1973).
[e] See Figure 5 in Kato et al. (1999, K99).
[f] See Figure 7 in Nyman et al. (1989, N89).

Table 2
Observed Coalsack Transitions

Molecule	Transition J	ν_0 (MHz)	Cores	V_{res} (km s^{-1})	σ_{rms} (10^{-1} K)	$\int \sigma_{\mathrm{rms}}$ (10^{-2} K km s^{-1})
^{12}CO	1–0	115271.202	C1–C7	0.08	1.47	7.19
^{13}CO	1–0	110201.353	C1–C7	0.09	1.28	4.46
C^{18}O	1–0	109782.173	C1–C7	0.09	0.84	4.14
HCO$^+$	1–0	89188.526	C2, C4	0.11	0.69	4.49
CS	2–1	97980.953	C2, C4	0.10	0.45	3.70
SO	3–2	99299.905	C2, C4	0.10	0.46	2.45
C_2H	1–0	87316.925	C2, C4	0.12	0.50	2.85
CH_3OH	2–1	96741.377	C2, C4	0.10	0.38	2.34

Note. See Section 3.

important line—in ascending frequency HCO$^+$, CS, SO, and C^{18}O for each configuration, respectively—be given band center priority in order to avoid any ringing edge effects. The front end is an MMIC cryo-cooled 3/12 mm receiver with noise diode calibration and a typical system temperature (T_{sys}) of 180 K. T_{sys} is checked with a paddle (chopper wheel) and calibrated with an ambient load between schedules. Pointing accuracy is better than 9″, also checked between schedules with the nearby SiO maser R Car. The FWHM Mopra beam size at 110 GHz is 33″ and the main beam efficiency is 0.45 (Ladd et al. 2005).

Data are gridded and fit with the Gridzilla and Miriad (Sault et al. 1995) packages[6] after Livedata, an AIPS++ task, subtracts a linear baseline fit to emission-free channels. The spectra are T_{sys} weighted and gridded into a datacube with a 0$.\!'$55 Gaussian smoothing kernel, resulting in an angular resolution of 46″ and rms sensitivity of 0.08 K per channel for C^{18}O.

It must be noted that the partly Sun-induced baseline ripple seen in CH_3OH and SO averaged spectra in Figures 1 and 2 will compromise the reliability of associated integrated intensity maps and position–velocity (lV) diagrams in Figures 3 and 4, respectively. However, since other observed line emission of similar strength corroborates these intensity levels and positioning in velocity space, we choose to include them here.

[6] http://www.atnf.csiro.au/computing/software

3. ANALYSIS AND DISCUSSION

Table 1 lists the observed cores, their coordinates, observed size in a given line, and the equivalent optical extinction associated with the core in that line. ^{12}CO emission area at half-peak integrated intensity exceeds map size in all the cores. Table 2 lists the observed molecules, their transition, rest frequency, location, velocity resolution, single channel, and integrated (over emission width) standard deviations. Table 3 lists values of the optical depth, excitation temperature, column and volumetric density, non-thermal, three-dimensional, and one-dimensional virial velocity dispersion, virial and observed mass calculated from ^{13}CO and C^{18}O emission for each of the seven Coalsack cores. Table 4 lists core values in the same lines of the thermal to non-thermal pressure ratio, total pressure, kinetic and rotational index, specific angular momentum, Alfvén mach number, Jeans length, magnetic Jeans length, Jeans mass, magnetic Jeans mass, characteristic magnetic mass, and critical mass. The significance of these properties, their calculation, and implications for the Coalsack cores are described in the Appendix, while the most salient results are given below.

Examining Tables 3 and 4 along with Moment morphologies (Sections 3.1, 3.2, and 3.3), we find that C2, C4, and C6 are closest to the collapse. The ^{13}CO observations probe core surface layers with densities as low as ∼100 cm^{-3}, while those of C^{18}O trace core interiors ∼2 mag denser. The ^{13}CO A_v values listed in Table 1 are within 20% those found by Tapia (1973) and Kato et al. (1999) in outer layers of the globules, while those of C^{18}O (also representing averages over the extended cores)

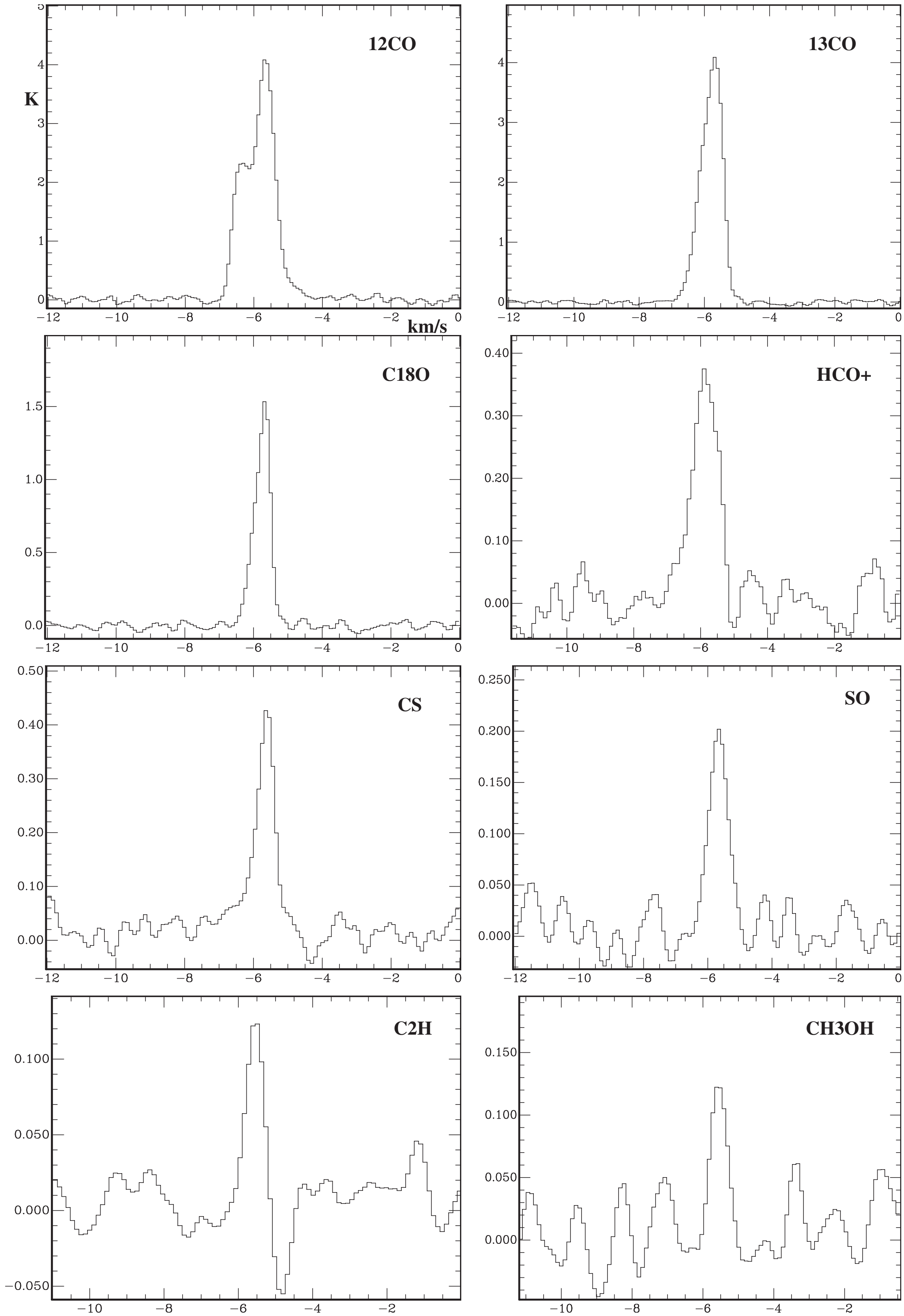

Figure 1. Coalsack C2 averaged spectra. Abscissa is LSR velocity, ordinate is $T_a{}^*$.

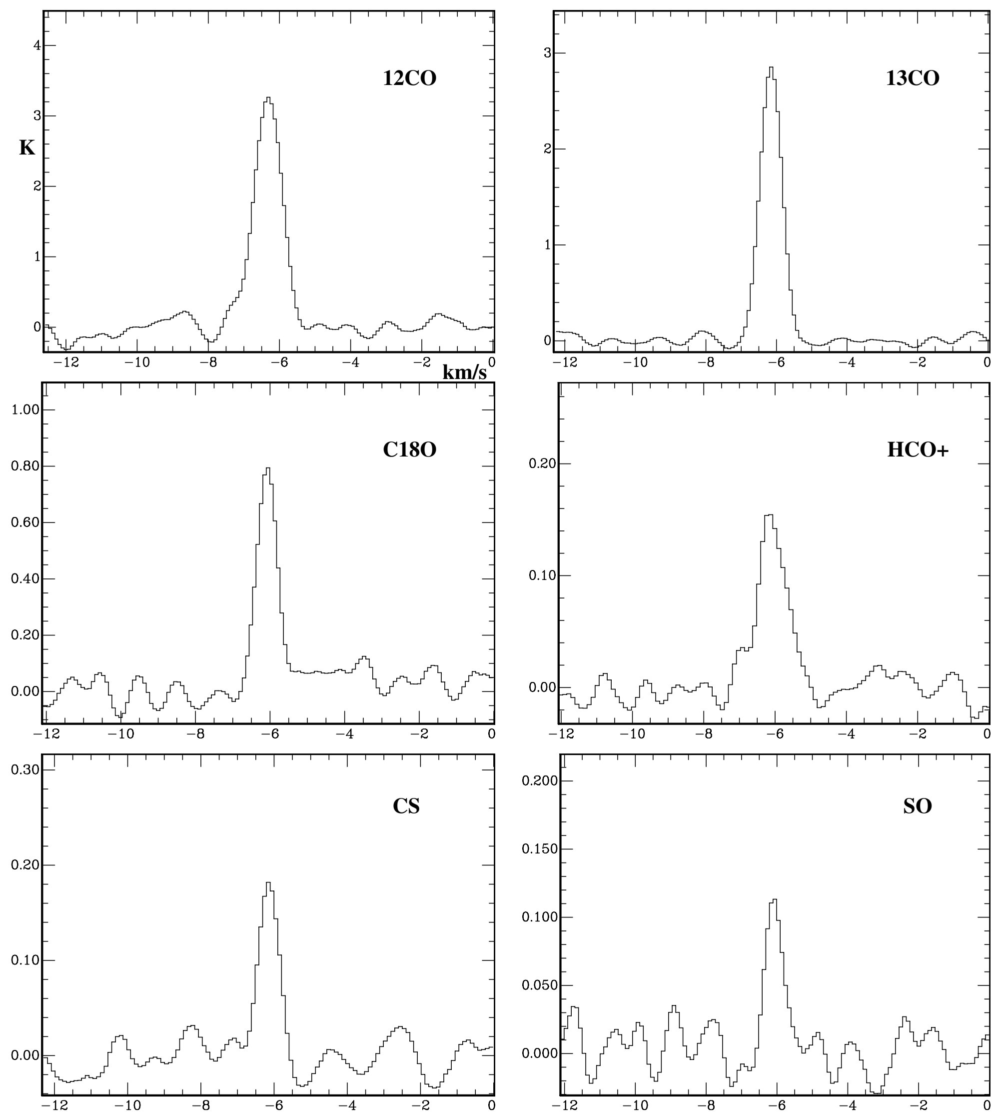

Figure 2. Coalsack C4 averaged spectra. Abscissa is LSR velocity, ordinate is $T_a{}^*$. Red wing in $C^{18}O$ profile signals outflowing motions.

Table 3
Physical Properties of Observed Coalsack Cores

Observed	τ	T_{ex} (K)	N (10^{15} cm^{-2})	$N(H_2)$ (10^{21} cm^{-2})	$n(H_2)$ (10^4 cm^{-3})	σ_{NT} (km s^{-1})	σ_{3D} (km s^{-1})	σ_{vir} (km s^{-1})	M_{vir} ($M_\odot$)	M ($M_\odot$)
C1:^{13}CO	0.72	6.7	3.42	2.7	0.44	0.38	0.62	0.14	21.0	2.4
C^{18}O	0.14	12.3	0.25	5.0	2.73	0.20	0.48	0.18	1.0	0.4
C2:^{13}CO	0.44	5.3	3.72	2.8	0.29	0.30	0.74	0.18	20.8	6.0
C^{18}O	0.10	13.4	0.51	6.5	1.61	0.17	0.44	0.11	4.9	2.4
C3:^{13}CO	0.51	5.1	2.10	2.2	0.36	0.28	0.59	0.13	10.3	2.0
C^{18}O	0.19	10.4	1.61	4.5	2.42	0.13	0.40	0.11	0.6	0.4
C4:^{13}CO	0.84	6.6	3.70	2.8	0.43	0.25	0.54	0.15	22.1	2.7
C^{18}O	0.15	12.4	0.27	5.2	1.92	0.15	0.42	0.13	1.5	0.9
C5:^{13}CO	1.05	7.1	3.12	2.6	0.42	0.34	0.67	0.14	17.9	2.3
C^{18}O	0.24	8.5	0.19	4.7	2.21	0.15	0.42	0.11	0.7	0.5
C6:^{13}CO	0.99	6.8	1.83	2.1	0.30	0.43	0.81	0.14	15.5	2.5
C^{18}O	0.18	6.8	0.20	4.8	1.90	0.26	0.56	0.12	2.1	0.7
C7:^{13}CO	0.98	5.7	1.63	2.0	0.32	0.32	0.64	0.12	17.0	1.8
C^{18}O	0.30	6.7	0.19	4.7	2.23	0.19	0.47	0.11	1.2	0.5

Notes. Values of the optical depth, excitation temperature, column and volumetric density, non-thermal, three-dimensional, and one-dimensional virial velocity dispersion, and virial and observed mass are listed. See Section 3.

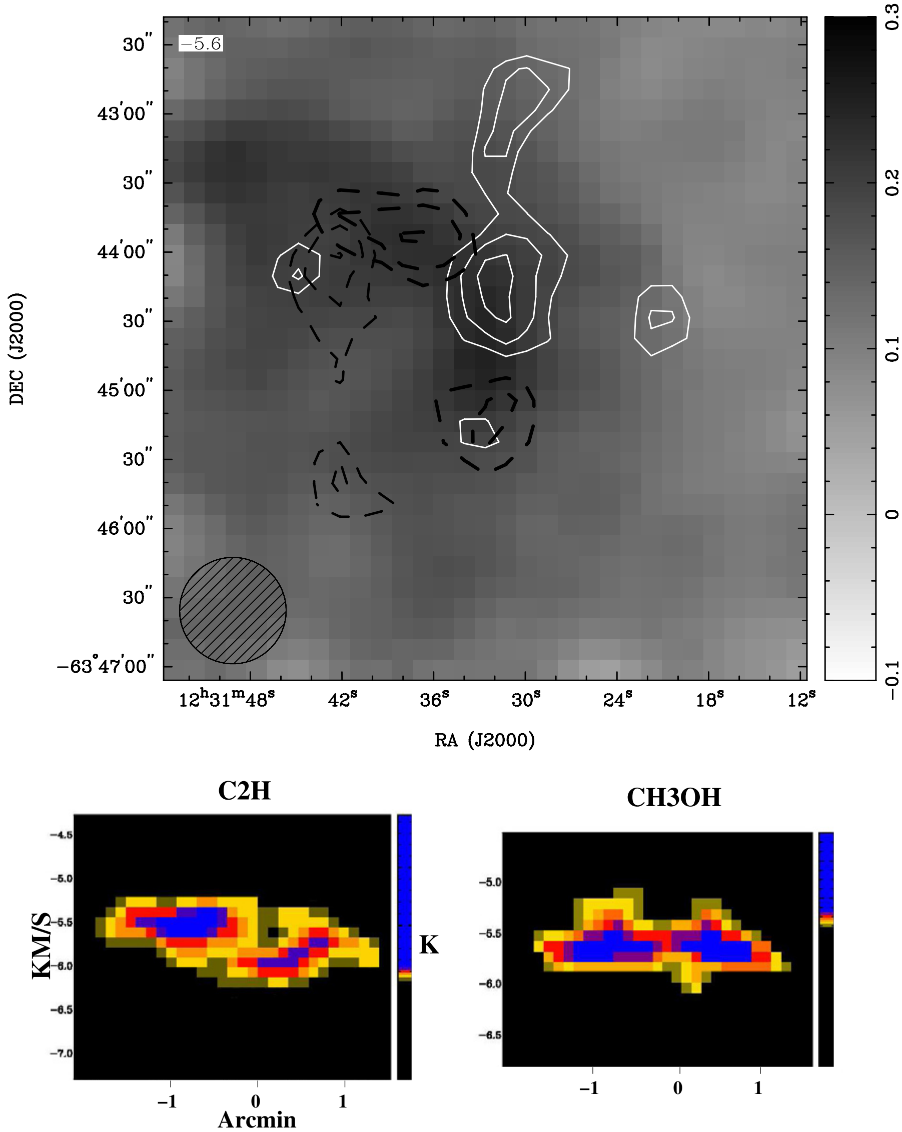

Figure 3. Top, C2 integrated intensities: CS gray scale in units of K km s^{-1} on SO (white), CH_3OH (thick broken), and C_2H (thin broken) contours in steps of σ starting at 3σ. Average velocity is given in upper left corner in km s^{-1}. The peak emission ring bounded by SO and C_2H NS aligned maxima (SO peak is within pointing accuracy of that of $C^{18}O$) to the W and E, respectively, indicates a beamwidth-sized (∼0.04 pc) central depletion region and follows the general morphology of the enhanced extinction ring discussed in Rathborne et al. (2009; e.g., Figures 5 and 8), only shifted $S \sim 0.02$ pc. Bottom: C2 core centered P.A. = 45° directed C_2H, CH_3OH lV diagrams. Intensity enhancements "blueward" (~ -6.0 km s^{-1}) of system velocity aligned with depletion are consistent with core centered outflowing motions. lV yellow and bluescales start at 3σ and 4σ, respectively.

(A color version of this figure is available in the online journal.)

are nearly a factor of three less than found in the center of C2 (Jones et al. 1984), indicating these observations do not probe the densest interiors. The observed paucity of dense gas around core regions is consistent with the lack of star formation in a chemically young Coalsack; a similar lack of activity in the presence of substantial gas mass is not entirely anomalous and has been observed in the Pipe Nebula (Onishi et al. 1999).

Jeans length (Λ_J) $C^{18}O$ values are close to the observed $C^{18}O$ emission indicated core diameter (L_{18}) in C2, C4, and C6; the magnetic Jeans length (Λ_{JB}) is closest of all cores to L_{18} in C6, surpassing Λ_J by only ∼30%. Since a (magnetic) core is susceptible to gravitational collapse when it reaches (Λ_{JB}) Λ_J, C2, C4, and C6 sizes are approaching collapse-critical values. Minimum and maximum Alfvén mach number (m_A) values are found in C3 and C6, respectively (see Appendix A.2); C6 may be undergoing fragmentation within an infalling envelope (Section 3.3) in a turbulent scenario (as opposed to C2 and C4, whose central region emission is quiescent—see Sections 3.1 and 3.2). The observed mass (M) of C2 approaches the Jeans value (M_J), while the rest of the cores are ∼half M_J. The magnetic Jeans mass (M_{Φ_B}) is ∼twice the observed mass of all the cores, again except in the case of C2, for which values are within 20%. The maximum value of the characteristic magnetic mass (M_B) is seen in C1 due to its strong (∼0.1 mG) field, the minimum belonging to C2, less than twice M. Thus, C2 may be nearing collapse. Critical mass (M_{CR}) values do not vary as much ($\leqslant$ factor of two) as M (> factor of three) in all the cores, consistent with prestellar objects approaching an equilibrium state (hydrostatic protostar). Cores with minimum and maximum values in the former case are C3 and C6, respectively, and in the latter, C7 and C2, while the values approach each other in C2, again indicating this core's proximity

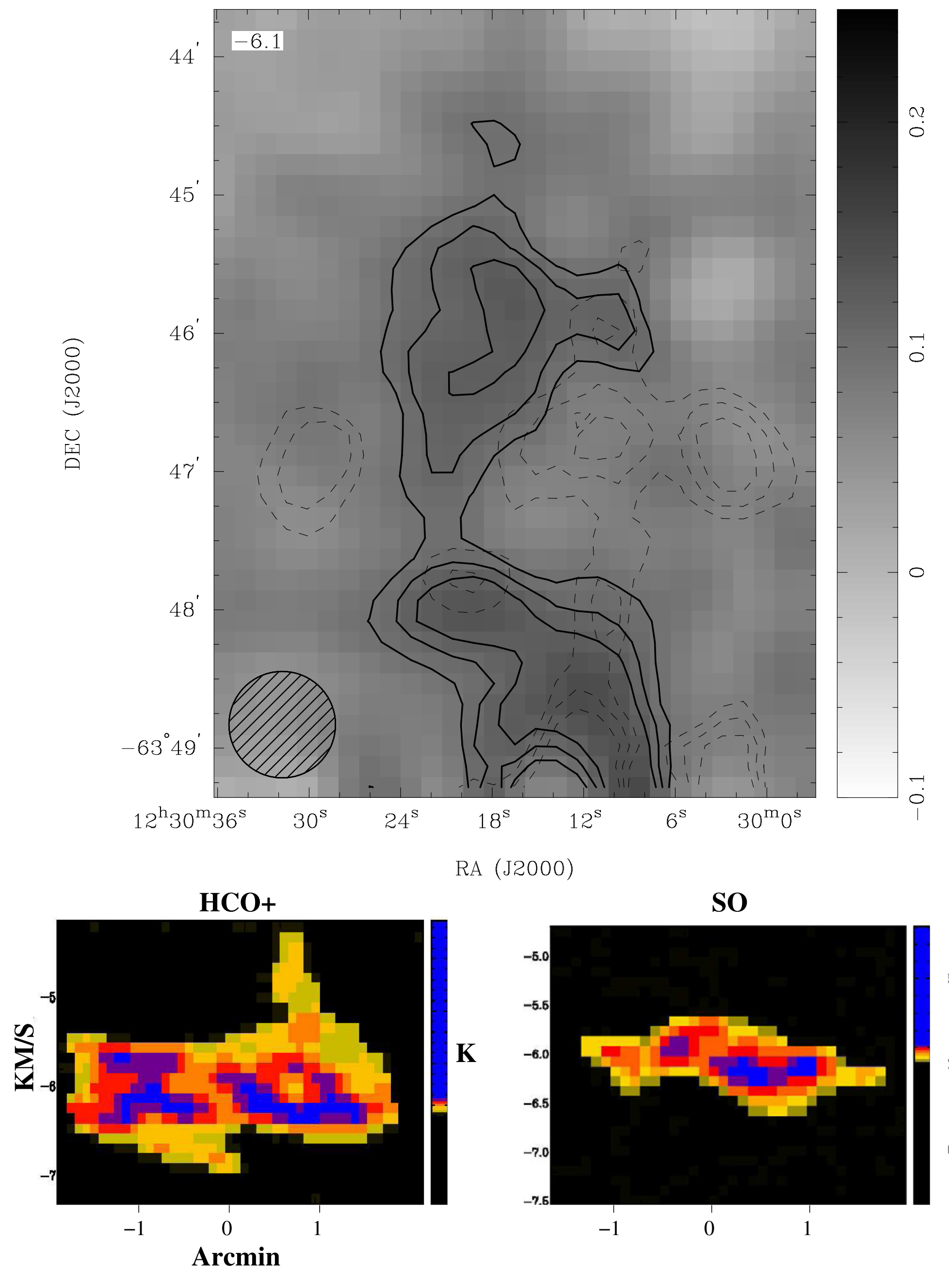

Figure 4. Top, C4 integrated intensities: CS gray scale in units of K km s^{-1} on CS (solid) and SO (broken) contours in steps of σ starting at 3σ. Average velocity is given in upper left corner in km s^{-1}. The intersection of optically thin emission filaments suggests a ∼0.03 pc diameter depletion zone in C4. Bottom, C4 core centered P.A. = 45° directed HCO^+, SO lV diagrams. lV yellow and bluescales start at 3σ and 4σ, respectively.

(A color version of this figure is available in the online journal.)

to collapse. Tables 3 and 4 values are consistent with significant magnetic field (e.g., Andersson & Potter 2005) support within prestellar cores; possibly a result of the interface with the energetic Upper Centaurus Loop plasma bubble bordering the Coalsack complex (Bhat & Andersson 2011).

Inherent uncertainties in the data due to differing distance estimates (150–240 pc—see Franco 1989; Seidensticker & Schmidt-Kaler 1989—180 pc used here), optical depth effects, saturation, as well as a possible anomalously low gas to dust ratio in the region (Kerr et al. 1976) make the true mass distributions difficult to determine. However, this latter effect would lower M, further decreasing likelihood of collapse and confirming these cores' prestellar nature.

The physical properties presented in Tables 3 and 4 describe not only cores which have not attained a star-forming critical mass despite having column densities (nearly 40% in the case of C2) above a fiducial minimum needed for star formation (∼4×10^{21} cm^{-2}) (Hara et al. 1999), but also the kinematic structure of neighboring cores, with ^{13}CO and $C^{18}O$ probed H_2 densities differing by a factor of ∼two, masses by a factor of ∼3–5, and virial masses by a factor of ∼20 (primarily due to larger ^{13}CO cores). Is this prestellar core differentiation in

Table 4
Physical Properties of Observed Coalsack Cores

Obs	P_{TNT}	$\log \frac{P_{\mathrm{tot}}}{\kappa}$ (K cm^{-3})	α	β	$-\log \frac{J}{M}$ (kms^{-1} pc^{-1})	m_A	Λ_J (pc)	Λ_{JB} (pc)	M_J (10 $M_{\odot}$)	M_{Φ_B} ($M_{\odot}$)	M_B ($M_{\odot}$)	M_{CR} (10 $M_{\odot}$)
C1:^{13}CO	0.3	4.7	8.8	0.72	2.2	2.4	0.26	0.29	7.4	3.7	8.8	7.8
C^{18}O	0.9	5.1	2.8	0.08	3.0	0.5	0.14	0.24	0.2	1.1	7.2	0.4
C2:^{13}CO	0.4	3.5	3.8	1.00	1.9	2.4	0.29	0.35	6.5	5.9	5.7	7.1
C^{18}O	1.2	4.8	1.7	0.03	2.6	0.6	0.21	0.41	0.4	2.9	4.2	0.7
C3:^{13}CO	0.5	4.0	6.7	0.81	2.2	2.0	0.25	0.39	5.5	3.1	7.4	5.8
C^{18}O	2.1	4.4	4.6	0.02	3.2	0.4	0.14	0.25	0.2	0.9	4.6	0.3
C4:^{13}CO	0.6	4.4	4.5	1.01	2.2	1.6	0.26	0.46	7.4	4.0	8.8	7.8
C^{18}O	1.6	4.8	3.4	0.03	2.9	0.5	0.17	0.31	0.3	1.7	5.5	0.5
C5:^{13}CO	0.3	4.6	7.7	1.12	2.2	2.3	0.28	0.36	8.3	3.6	8.8	8.7
C^{18}O	1.6	4.9	4.8	0.05	3.0	0.4	0.13	0.18	0.2	1.2	6.1	0.3
C6:^{13}CO	0.2	4.6	11.8	1.21	2.1	3.4	0.32	0.35	9.2	3.4	6.3	9.6
C^{18}O	0.5	5.1	8.0	0.14	2.9	0.8	0.13	0.17	0.1	1.3	4.5	0.3
C7:^{13}CO	0.4	4.5	8.9	2.23	2.1	2.4	0.28	0.33	6.8	2.7	6.1	7.1
C^{18}O	1.0	5.0	5.9	0.26	2.7	0.6	0.11	0.18	0.1	1.2	6.1	0.2

Notes. Values of the thermal to non-thermal pressure ratio, total pressure, kinetic and rotational index, specific angular momentum, Alfvén mach number, Jeans length, magnetic Jeans length, Jeans mass, magnetic Jeans mass, characteristic magnetic mass, and critical mass are listed. See Section 3.

concert with similarity in the above values in any one line in all cores but C2 (e.g., $N(H_2)$ in C^{18}O for the six cores differs by a maximum of ~10%—see Table 3) a sign that the initial conditions for star formation are stabilizing (i.e., established) at this early stage? Let us examine in more detail the candidates closest to the collapse: C2, C4, and C6.

3.1. C2

^{12}CO decentralized intensity enhancements and dual IV maxima show evidence for central depletion (Figures 5 and 6). ^{13}CO and C^{18}O line profiles (S/N ~50) do not show any absorption dip from peak to wing (Figure 1), and there are blue wings with truncated red emission in ^{12}CO, ^{13}CO, and HCO^{+} emission consistent with infall (e.g., Carolan et al. 2009). The lack of strong rotation and outflow signatures (Figure 6) again impels us to consider the presence of infalling motions associated with the skewed profiles.

The narrow-line component width in ^{12}CO emission, 0.60 km s^{-1}, is the smallest of all ^{12}CO lines in the seven cores despite the 90% peak integrated intensity contour velocity dispersion of 0.41 km s^{-1} (considerable in the Coalsack), signaling a turbulence embedded quiescent clump, which shows signs of weak rotation with a velocity gradient of ~0.7 km s^{-1} pc^{-1}. This NS gradient runs map length (~0.37 pc) and experiences a δ_{J2000} ~ −63 44 30 centered reversal (passing ~0.01 pc south of peak brightness), corresponding to an EW flow axis coincident with a dispersion ridge following peak emission; a flattened dispersion minima region lies just south in the depleted core center (Figure 6). As seen in the same figure, polar isovelocities merge perpendicularly to a pinch further east at α_{J2000} ~ 12 31 44, coinciding with an abrupt (changing flux rapidly) central ridge of CS integrated intensity, which leads NW ~0.01 pc to an NS gradient reversal bridge coinciding with a dispersion ridge. This is consistent with an accretion stream which has its origins in relative quiescence, 0.30 km s^{-1} less dispersive than outlying regions and half the width of the narrow-line component itself. This bright stream is apparent in an IV peak (−5.75 to −5.67 km s^{-1}) intensity strip of ~20:1 aspect ratio in ^{13}CO (and in CS) emission (Figure 6).

In ^{13}CO, C2 is the only core in this study whose total pressure is greater than that of the entire Coalsack Nebula (see Appendix A.1). As seen in Figure 6, there is a 90° radial velocity shift to the north and south of central emission, marking perpendicular flows which merge at the equator; similar behavior in C^{18}O is noted by Rathborne et al. (2009). The ~0.8 km s^{-1} pc^{-1} velocity gradient undergoes an NS reversal along the same EW axis as in ^{12}CO, signaling an equatorial flow aligned with peak dispersion and integrated intensity. ~0.01 pc to the south, a flattened velocity dispersion minimum at α_{J2000} = 12 31 33, coincident with CS and SO emission peaks as well as a central HCO^{+} dispersion minimum, marks a central core dissipation of turbulence (Figure 6).

HCO^{+} depletion is coincident with CS and SO emission centers. Also in Figure 6, the eastern integrated intensity maximum extends into peak dispersion regions of 0.30 km s^{-1}, where EW radial velocity bridges disintegrate, and the intensity distribution flattens; this region coincides with a similar abrupt 90° shift in SO velocity, indicating the presence of a polar aligned flow. This dual flow is consistent with emission profiles exhibiting a red- and blue-tilted (with respect to center velocity) FWHM and peak, respectively (Figure 1).

C_2H and CH_3OH exhibit velocity dispersion maxima around integrated intensity depletions; the former non-thermal value is 0.19 km s^{-1}, that of the H_2 thermal width at ~10 K, marking a pressure balance in core regions. An NS radial velocity gradient is present, and EW running isovelocities coinciding with central dispersion minimization are consistent with the presence of an accretion plane and inner core turbulence dissipation, respectively. Considering these at the position of (^{12}CO, ^{13}CO, and C^{18}O) flow convergence (as noted above) within a core exhibiting critical collapse-shy indices (Tables 3 and 4), this scenario is consistent with "outside-in" evolution in C2 as suggested by Rathborne et al. (2009), whose central regions are condensing further, prior to subsequent "inside-out" collapse, as described by Shu et al. (1987).

3.2. C4

^{12}CO has the smallest line width and velocity dispersion of the Coalsack cores studied, suggesting turbulence to be relatively insignificant. However, rotation may be important as the velocity gradient is ~1.2 km s^{-1} pc^{-1} (second highest after C7 and twice that of C2); core morphology reflects the resultant torque in a

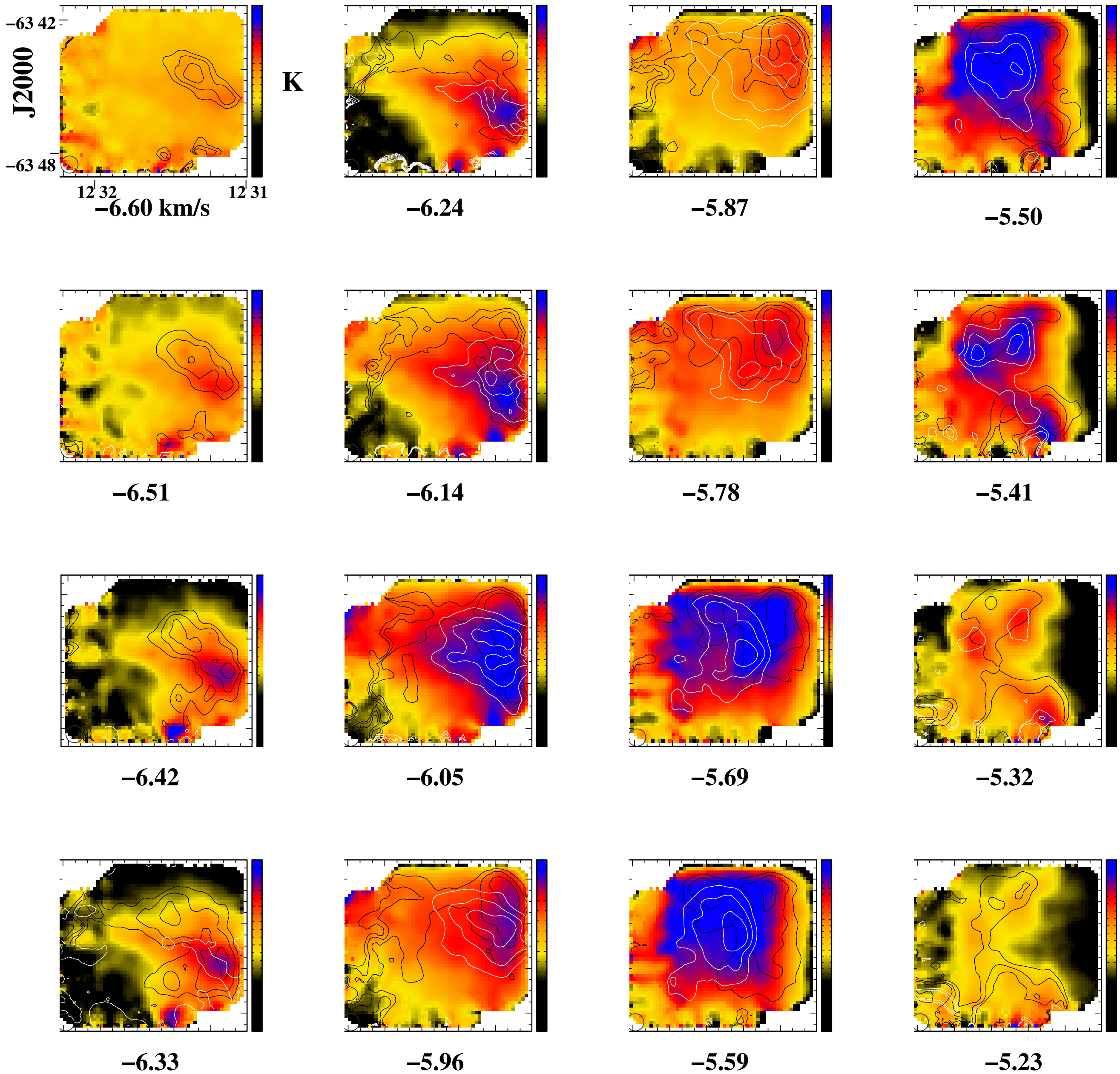

Figure 5. C2 sequential channel maps: ^{13}CO pixels on black ^{12}CO and white C^{18}O peak intensity contours in steps of σ. ^{12}CO and C^{18}O have minimum contours of 20σ and 10σ, respectively. The relative intensity scale is constant; blue scale starts at a minimum of $5\sigma = 0.64$ K. Note C^{18}O emission peaks in regions of ^{12}CO depletion.

(A color version of this figure is available in the online journal.)

twisted NS emission lane, and there is a continuous NNE–SSW radial velocity gradient extending map length ($\sim$0.26 pc) evident in other species' emission as well (Figures 7 and 8). In the rest of the Coalsack cores, ^{12}CO has a weaker gradient than that of ^{13}CO or C^{18}O (as expected with a larger radius); in C4 the gradient is stronger, indicative of this gas shell's high angular momentum, and likely accentuating the significance of the contrasting C^{18}O properties discussed below. Dispersion isocontours run perpendicular to the prominent NWW–SEE flow axis as in ^{13}CO emission (Figure 8), suggesting flow displacement dependent turbulence, with maximum dispersive values of 0.45 km s^{-1} coinciding with the central emission peak.

The Coalsack cores in ^{13}CO emission all exhibit super-Alfvénic velocity dispersions except in the case of C4 (0.26 km s^{-1}). N and P_{TNT} are the highest of the ^{13}CO cores as is M_{vir}, indicating the possible initiation of collapse on the one hand, and the presence of unbounded motions on the other. As seen in Figure 9, peak integrated intensity contours in all three species trace out a line across a ring of C^{18}O velocity dispersion maxima, two peak ^{13}CO emission regions straddling the local minimum contributing to its broad profile. The brighter northern one, at $\delta_{J2000} \sim -63\ 46\ 00$, coincides with northern CS and C^{18}O integrated intensity peaks and is aligned with dispersion contours directed along the velocity field indicated flow axis perpendicular to the predominant NNE–SSW contours, consistent with accretion plane presence there (Figure 8).

P_{TNT} in C4 is the highest of the Coalsack cores, suggesting C4 self-gravity to be least impeded by internal turbulence of all the cores toward potential collapse. A large-scale NS

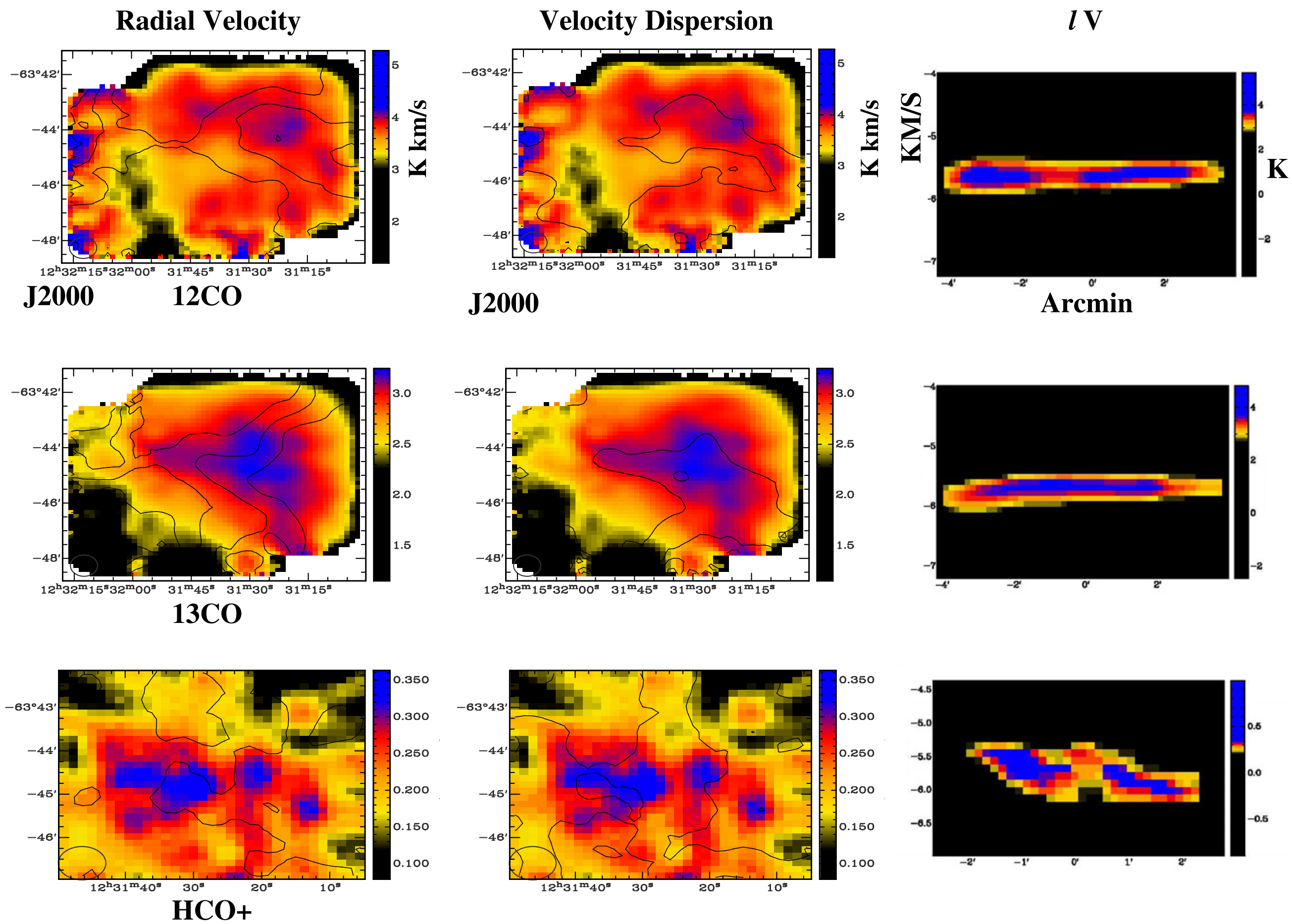

Figure 6. Coalsack C2: integrated intensities on Moments 1 and 2 contours followed by lV slices across the core center directed with a position angle (P.A.) of 45°. ^{12}CO Moment 1 contours: -5.88, -5.82, and -5.76 km s^{-1}; Moment 2: 0.42 km s^{-1}; ^{13}CO 1: -5.84, -5.77, and -5.70 km s^{-1}; 2: 0.30 km s^{-1}; HCO$^+$ 1: -5.80 km s^{-1}; 2: 0.24 km s^{-1}. lV bluescale starts at 40σ, 40σ, and 4σ. Radial velocity reversals and central dispersion minima coincident with flattened lV peak intensities and depletion zones are indicative of the growing importance of accretion.

(A color version of this figure is available in the online journal.)

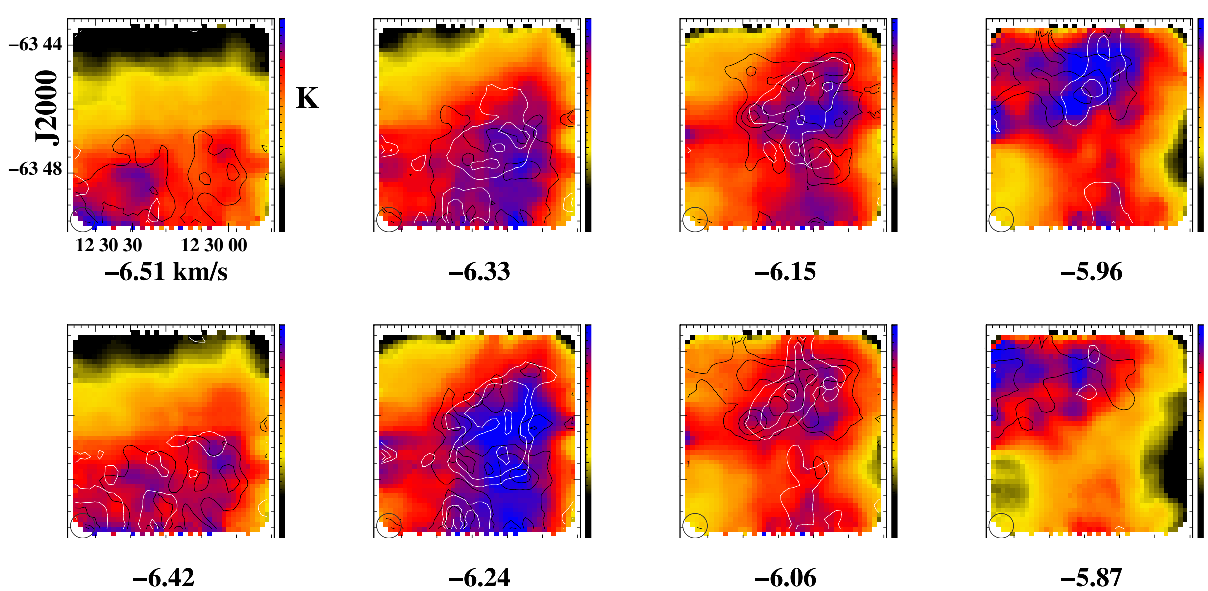

Figure 7. C4 channel maps: ^{13}CO pixels on black ^{12}CO and white C^{18}0 contours. ^{12}CO and C^{18}O have minimum contours of 20σ and 8σ, respectively. The relative intensity scale is constant; bluescale starts at a minimum of $20\sigma = 2.56$ K. Note decentralized peak intensity (marking depletion) NS shift; ^{13}CO maxima trace out a ring.

(A color version of this figure is available in the online journal.)

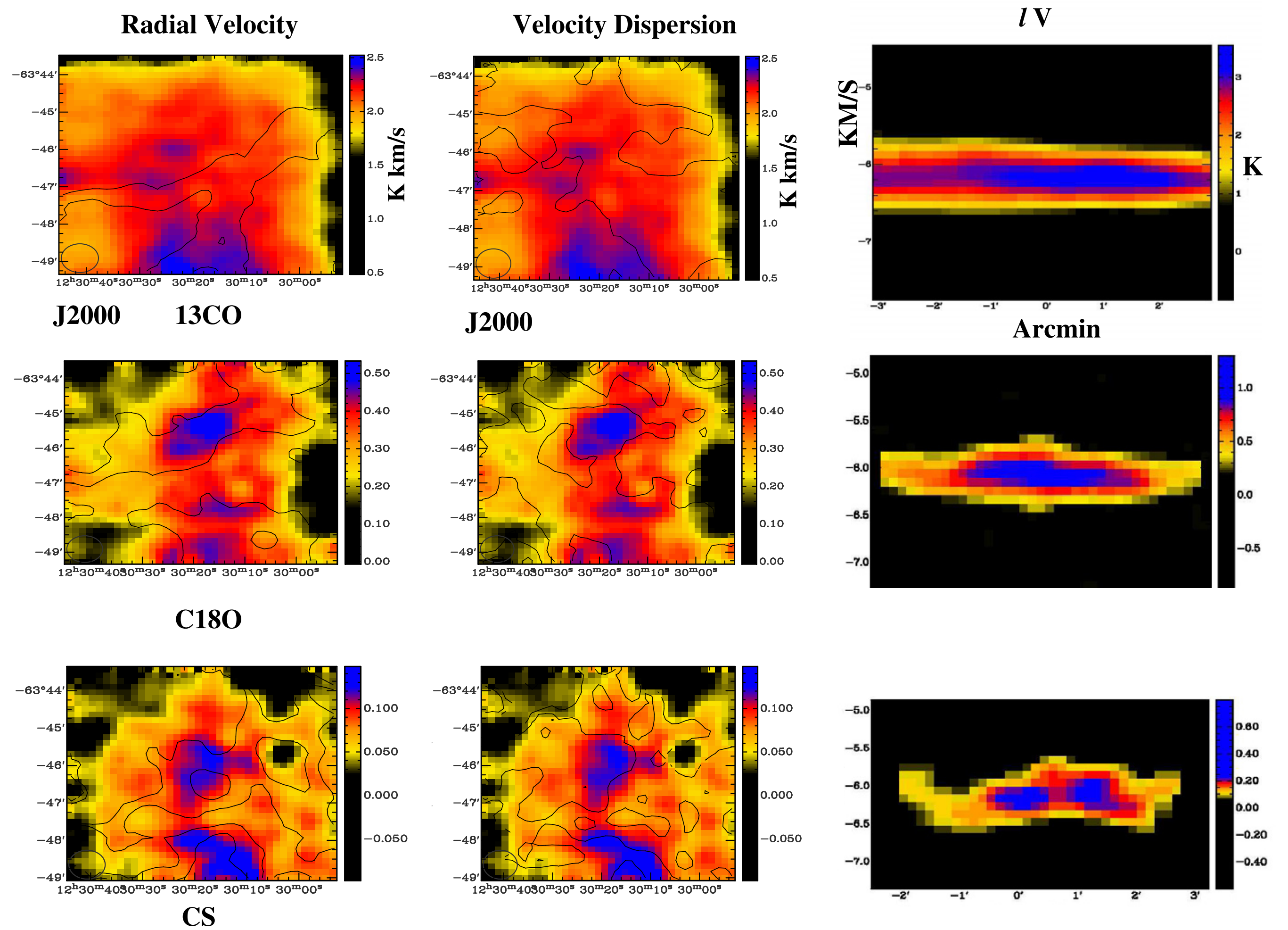

Figure 8. Coalsack C4: integrated intensities on Moments 1 and 2 contours followed by lV slices across the core center directed with a P.A. of 45°. ^{13}CO Moment 1 contours: −6.2 and −6.1 km s^{-1}; Moment 2: 0.26 and 0.29 km s^{-1}; C^{18}O 1: −6.1 and −6.0 km s^{-1}; 2: 0.16 and 0.19 km s^{-1}; CS 1: −6.15 and −6.05 km s^{-1}; 2: 0.13 and 0.17 km s^{-1}. lV bluescale starts at 30σ, 10σ, and 3σ. The NNE–SSW velocity gradient and perpendicular dispersion gradient decrease from ^{12}CO to C^{18}O are consistent with a growing importance of outflowing motions as are core centered lV $\sim 4\sigma$ bipolar enhancements.

(A color version of this figure is available in the online journal.)

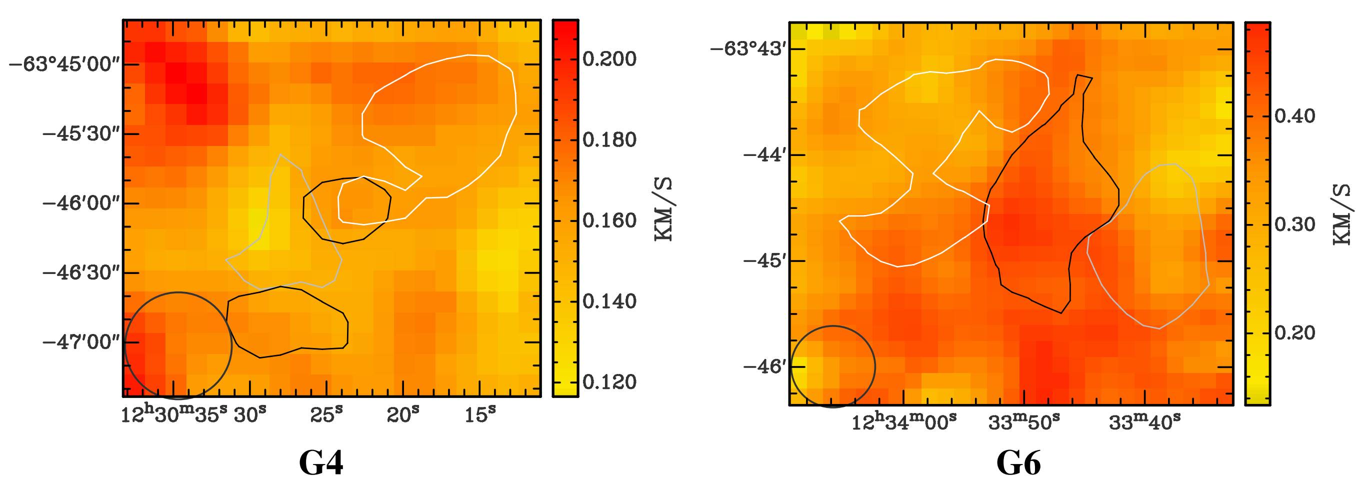

Figure 9. C^{18}O C4, C6 velocity dispersion pixels on 7σ+ C^{18}O (white), ^{13}CO (black), and ^{12}CO (gray) integrated intensity contours. C4 emission lies across a ring of dispersion maxima; C6 lies emission across flattened maxima ∼bisected by the ^{13}CO distribution which is aligned with polar region dispersion enhancements.

(A color version of this figure is available in the online journal.)

velocity dispersion gradient is discontinuous along the central emission lane, with peak integrated intensity relative values (increase and decrease to the west and east, respectively—see Figure 8—rather than aligned as in ^{13}CO) likely due to mixing of turbulent and quiescent regimes, evident in the significant dispersion scatter, up to half the peak emission region maximum value of 0.19 km s^{-1} in ∼0.03 pc. C^{18}O lV emission reveals two flattened intensity maxima (each with an aspect ratio of 4:1) separated just over resolution by ∼0.1 km s^{-1}, centered at 30″ offset, whose polar regions exhibit a slight intensity increase, four pixels each above 3σ, consistent with outflow initiation (Figure 8).

As seen in Figure 8, CS emission reveals an NWW–SEE flow (notably similar to that in ^{13}CO and C^{18}O) running between the two integrated intensity peaks; a dispersion valley extends map length in the same region. There is a radial velocity minimum ∼0.01 pc south of the northern integrated intensity peak and coincident with the depleted midpoint of the two C^{18}O peaks; the position and orientation of this flattened gradient reversal is consistent with a stalling of infalling gas upon fragmentation, supported by its emission's significant blue profile wings (Figure 2). This region is ∼0.02 pc from dispersion minima to the east and south, the latter coincident and aligned with a −6.10 km s^{-1} isovelocity bottleneck, consistent with the presence of an accretion plane as noted above. SO (Figure 4), C_2H, and CH_3OH morphologies seem to confirm an effective ∼5000 AU inner envelope edge, whose approximate age of 8″/3.0 km s^{-1} ∼2300 years (outflowing emission extent/corresponding C^{18}O line center-wing deviation—see Figure 2) assuming constant velocity of outflowing motions at a distance of 180 pc, places C4 in an extremely young position.

3.3. C6

C6 spectra and morphologies are indicative of core centered infalling motions. All profile peaks are blueshifted with respect to center velocity (Figure 10), and channel maps suggest a converging of component clumps and associated flows. ^{12}CO, ^{13}CO, and C^{18}O have the greatest line widths and velocity dispersions of all core emission in this study. ^{12}CO and ^{13}CO have the greatest integrated intensities; their red shoulders correspond to that portion of infalling material moving away from our line of sight.

As in ^{12}CO and C^{18}O emission, radial velocity and dispersion field values in ^{13}CO reveal a general anticorrelation, with more negative velocities corresponding to higher dispersions. The exception occurs in a region comprising an NEE–SWW radial velocity bridge passing through peak integrated intensity, where systemic velocities are aligned with the supersonic, twice-Alfvénic dispersion distribution (Figure 11). The surrounding equatorial turbulent feature has a major axis centered on δ_{J2000} = −63 45 00 and extends ∼0.10 pc, with a substantial ∼0.03 pc width above the 0.50 km s^{-1} level. Also seen in Figure 11, its peak of 0.53 km s^{-1} is ∼0.01 pc south of peak integrated intensity, where perpendicular isovelocity convergence may mark an active site of fragmentation. The NEE–SWW flow running through peak integrated intensity and that perpendicular aligned with dispersion contours to the east correspond to flattened peak lV emission and its depletion-centered bipolar enhancements, corresponding to accretion and outflow planes, respectively (Figure 11). That the minimum velocity "hole" at the intersection of these two planes coincides with C^{18}O peak integrated intensity seems to support this scenario.

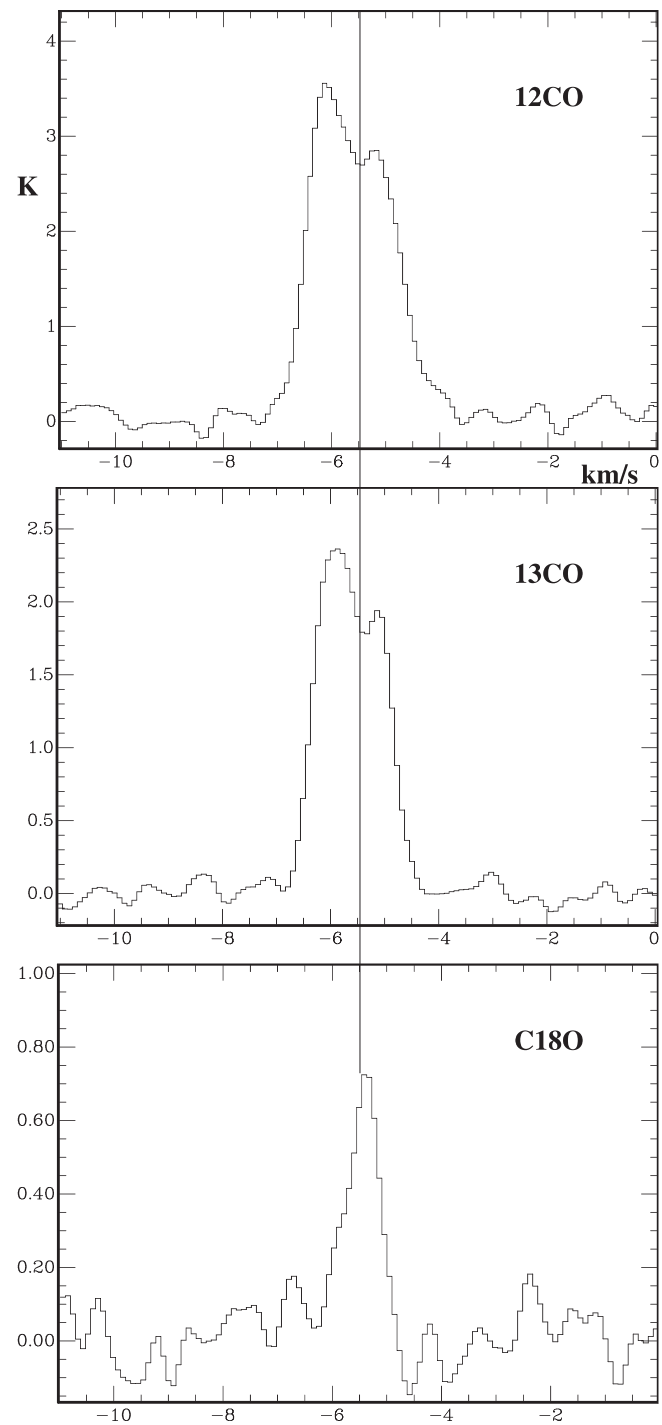

Figure 10. Coalsack C6 box (∼0.04 pc side^{-1}) averaged spectra centered on α_{J2000}, δ_{J2000} = 12 33 50, −63 44 30; this point is the maximum integrated intensity center which is ∼0.01 pc from maximum dispersion in ^{13}CO and C^{18}O, ∼0.03 pc from that in ^{12}CO. Abscissa is LSR velocity, ordinate is T_a*. Redshifted (with respect to peak) absorption dips in ^{12}CO and ^{13}CO profiles coincident with optically thin C^{18}O peaks at systemic velocity suggest infall.

4. CONCLUSIONS

The dense molecular cores in the Coalsack Nebula are of great interest in studies of early star formation. Despite being exposed to the star formation triggering nature of the galactic plane, they appear largely quiescent with a lack of outflow.

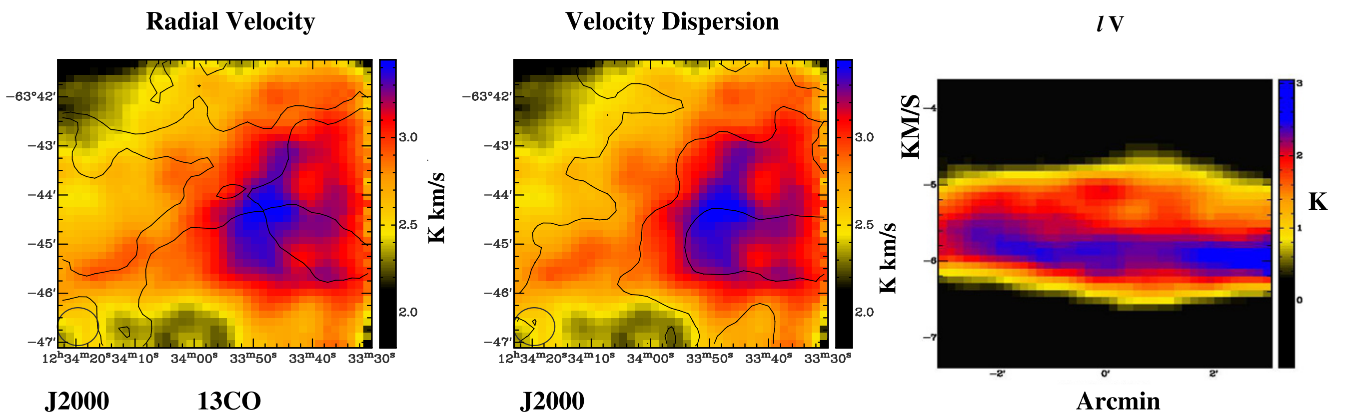

Figure 11. Coalsack C6: ^{13}CO integrated intensity on -5.60 and -5.55 km s^{-1} Moment (1), and 0.36, 0.43, and 0.50 km s^{-1} Moment (2) contours followed by lV diagram. lV bluescale starts at $\sim 20\sigma$. Perpendicular isovelocities converge at peak integrated intensity, which confirms flattened peak dispersion contours $\sim$0.01 pc south.

(A color version of this figure is available in the online journal.)

1. Critical mass calculations are consistent with the presence of magnetic field support within these prestellar cores; C2, C4, and C6 values place them closer to the collapse.
2. In these three cores, radial velocity flow reverses across a plane perpendicular to emission exhibiting outflowing motions. Along with blue-skewed emission profiles, this is consistent with accretion on to an equatorial disk. We observe central core region dispersion minima in C2, aligned local minima in C4, and aligned maxima in C6. This in turn is consistent with C2 and C4 experiencing a turbulence decay in a subsonic core within perpendicularly merging CO flows, while in C6 there is a growth of turbulence in a supersonic core.
3. In C6, the most turbulent of the observed cores, emission centroid velocities decrease at peak integrated intensity, $\sim$0.01 pc from peak velocity dispersion. Together with redshifted (with respect to peak) absorption dips in ^{12}CO and ^{13}CO profiles coincident with optically thin C^{18}O peaks at systemic velocity, this is consistent with fragmentation within an infalling envelope.

Using the Mopra narrowband MOPS digital filterbank, we have produced images with sufficient spectral resolution (80 m s^{-1}) to probe the Coalsack cloud chemistry and kinematics on small scales (0.01 pc), to determine that the molecular cloud cores are not massive enough for global collapse. However, three of the densest cores (C2, C4, and C6) may be on the brink of protostar formation.

We thank the ATNF at CSIRO for support of the Mopra telescope and facilities. We also thank the referee for comments which improved this paper.

APPENDIX

A.1. Turbulence

Dissipation of internal core turbulence may be crucial in determining star-forming potential (e.g., Nakano 1998); the ability of turbulence to provide support against gravitational collapse is suggested in numerical studies to be effective as long as the energy injection scale at core densities is smaller than the Jeans length (Klessen et al. 2000). The average three-dimensional velocity dispersion is $\sigma_{\rm 3D} = \sqrt{3{c_s}^2 + 3{\sigma_{\rm NT}}^2}$, where the one-dimensional isothermal sound speed for hydrogen at 10 K, $c_s = 0.188$ km s^{-1}, $\sigma_{\rm NT} = \sqrt{\sigma^2 - {\sigma_T}^2}$, where σ is the average velocity dispersion measured from the second Moment maps, and the thermal velocity dispersion, $\sigma_T = \sqrt{\frac{\kappa T_k}{m}}$, is 0.05 km s^{-1} for C^{18}O. $\sigma_{\rm 3D}$ is less than the escape velocity, $\sqrt{\frac{2GM}{R}}$, for all seven cores, implying that the cores are (marginally) gravitationally bound. Radii used are the distances from peak integrated intensity to that at which average values are halved. The one-dimensional virial dispersion, $\sigma_{\rm vir} = \sqrt{\frac{GM}{5R}}$, is lower than both the measured dispersion σ and sound speed, indicating that the globules are not virialized. Non-thermal velocity dispersions are supersonic (but sub-Alfvénic) for C1 and C6, which also have the highest gas pressures. The ratio of thermal to non-thermal support, $P_{\rm TNT} = \frac{c_s^2}{{\sigma_{\rm NT}}^2}$, gives an idea of how important a role turbulence plays in core internal pressure support and is around unity for C1, C2, and C7, suggesting equipartition between turbulent and thermal core energies. The thermal pressure is twice the non-thermal contribution for C3 while the situation is reversed for C6 signifying the former's gravitational susceptibility due to weak turbulent support and the latter's lack thereof. We find the total gas pressure as the sum of thermal and non-thermal contributions, $P_{\rm tot} = \rho({c_s}^2 + {\sigma_{\rm NT}}^2)$ where the average density $\rho = \frac{3M}{4\pi R^3}$. We note the comparison of this value with that of the overall ISM confining pressure, $P_{\rm ISM}/\kappa \sim 10^4$ K cm^{-3} (Bertoldi & McKee 1992) and that of the entire nebula given by $P_{\rm neb} = \frac{3\pi}{20} pG\rho_s$, where ρ_s is the mean surface density $\rho_s = \frac{M}{\pi R^2}$ and p is the apparent aspect ratio of the major to minor axes, $\sim$1.6 here. Adopting Nyman et al. (1989) values for the total Coalsack gas mass of 3550 $M_\odot$ and a length of 7.1 pc gives $P_{\rm neb} = 0.8 \times 10^4$ K cm^{-3}, slightly less than that of the ISM and less than all seven cores here in ^{13}CO with the exception of C2 because of its considerable size. The compact C^{18}O cores contain more pressure than both the ISM $P_{\rm ISM}/\kappa \sim 10^4$ K cm^{-3} and nebula's $P_{\rm neb} = 0.8 \times 10^4$ K cm^{-3} confining weight combined by a factor of $\sim$five except in the case of C3 which has the non-thermal velocity dispersion ($\sim$0.13 km s^{-1}) of all the cores. The dimensionless virial parameter α gives the relative importance of kinetic and gravitational energies, $\alpha = \frac{5\sigma^2 R}{GM} = \frac{2T}{W}$ where the kinetic energy $T = \frac{3}{2}\int_V \rho({c_s}^2 + {\sigma_{\rm NT}}^2)\, dV = \frac{3}{2}P_{\rm tot}V$ and the gravitational energy $W = -\frac{3GM^2}{5R}$, where $G = \frac{1}{232}M_\odot$ km s^{-1} pc^{-1}. The fact that cores typically evolve in an environment in which the dynamical scale is longer that the constituent free-fall and signal crossing times (e.g., Bertoldi & McKee 1992) allows us to say, for $\alpha \gg 1$, cores are surface-pressure-confined and self-gravity is insignificant ($T \ll W$) while for $\alpha \sim 1$ gravity becomes comparable to the kinetic energy. Larger α values (C1, C6, and C7) reveal strong internal pressure against the ambient medium, not necessarily virial imbalance. α reflects gravity's significance in C2 and conversely in C6 for which the maximum ($C^{18}O$ core) Coalsack value $\alpha \sim 8$ marks kinetic energy prevailing mostly due to its large non-thermal velocity dispersion. The dimensionless parameter β gives the relative importance of rotational to gravitational energies:

$$\beta = \frac{(1/2)I\omega^2}{qGM^2/R} = \frac{p\omega^2 R^3}{2qGM},$$

where q is defined so that the gravitational potential is $\frac{qGM^2}{R}$, p such that the moment of inertia $I = pMR^2$, and $\omega = \frac{dv}{ds} / \sin i$. Assuming a spherical r^{-2} density profile, $\frac{p}{q} = 0.22$, $\sin i = 1$ (e.g., Goodman et al. 1993), and $\frac{dv}{ds}$ is the linear velocity gradient measured from the first Moment map across each core. The ^{13}CO cores' larger β values reflect their retaining of angular momentum mainly due to greater size. The importance of rotation is seen in C7 with $\beta = 0.26$ and to a lesser extent C6 ($\beta = 0.14$); for the rest of the cores, gravitational energy dominates that of rotation ($\beta \ll 1$). C7's 4.2 $\mathrm{km\,s^{-1}\,pc^{-1}}$ gradient corresponds to a solid body rotation axis perpendicular to the line of sight of angular velocity $1.36 \times 10^{-13}\ \mathrm{s^{-1}}$, almost an order of magnitude greater than that of C2 and C4 ($\omega = 3.2, 3.6 \times 10^{-14}\ \mathrm{s^{-1}}$, respectively). Specific angular momentum is calculated by $\frac{J}{M} = p\omega R^2$, where angular momentum $J = I\omega$. The ^{13}CO clump values vary little and are a factor of ∼five higher than for the $C^{18}O$ cores, for which low C2 and C7 values (see Table 2) are due to greater size and velocity gradients, respectively.

A.2. Magnetic Field

Another major factor in core support is the magnetic field. The Alfvén mach number expresses core turbulence in terms of the characteristic Jeans and Magnetic masses:

$$m_A = \frac{\sigma\sqrt{3}}{v_A} = 0.843 \left(\frac{Z}{R}\right)^{-2/3} (\rho)^{-1/6} \left(\frac{M_J}{M_B}\right)^{1/3}$$

for a spherical clump where the Alfvén velocity,

$$v_A = \frac{B}{4\pi\rho} = 1.1 \frac{B}{\mu\mathrm{G}} \left(\frac{n}{\mathrm{cm}^3}\right)^{-1/2},$$

provides an estimate of the magnetohydrodynamic (MHD) contribution to the observed line width and $\frac{Z}{R}$ is the aspect ratio. The Jeans length

$$\Lambda_J = \sqrt{\frac{\pi(c_s)^2}{G\rho}} = \sqrt{\frac{\pi\kappa T}{Gn(\mu m_H)^2}} = 6.7\sqrt{\frac{T}{n}}$$

is the size limit above which the non-magnetic core will become gravitationally unstable, where $\rho = \mu m_H n$ and $\mu = 2.33$ is the mean molecular hydrogen mass. C2 and C4's Jeans lengths are close to the observed coherent core radii while for the rest of the ^{13}CO cores, the values are one-third higher. Λ_J corresponds to the Jeans mass

$$M_J = \frac{\pi\rho}{6}(\Lambda_J)^3 = \frac{\pi\mu m_H n}{6}\left(\frac{\pi\kappa T}{Gn(\mu m_H)^2}\right)^{3/2} = 9T^{3/2}n^{-1/2}\,M_\odot,$$

which for the less dense ^{13}CO cores is substantial as expected. The magnetic Jeans length accounts for the Alfvénic velocity and subsequent magnetic support:

$$\Lambda_{\mathrm{JB}} = \sqrt{\frac{\pi\left({c_s}^2 + {v_A}^2\right)}{G\rho}}$$

and is just a little more than the non-magnetic Jeans length due to the weak field permeating the ^{13}CO cores. The magnetic field is calculated with the ratio of the average velocity dispersion σ and polarization angle dispersion σ_Θ (Chandrasekhar & Fermi 1953):

$$\mu B = \frac{\sigma}{\sigma_\Theta}\sqrt{4\pi\rho},$$

which adapted to the Coalsack gives (Rathborne et al. 2009):

$$B = 10\sqrt{\frac{n(\mathrm{H_2})}{2700}}\,\mu\mathrm{G}$$

making use of the polarization dispersion measured by Jones et al. (1984) of $\sigma_\Theta = 0.66$ rad where the hydrogen number density $n(\mathrm{H_2})$ is in $\mathrm{cm^{-3}}$. The magnetic analog to the Jeans mass, $M_{\Phi_B} = 0.12\frac{\Phi}{\sqrt{G}}$ represents the maximum stable core mass with a magnetic flux $\Phi = \pi R^2 B$, the coefficient taken from MHD calculations (Tomisaka et al. 1989) for an ellipsoid mass distribution threaded by a uniform field. M_{Φ_B} is independent of core density; in the absence of ambipolar diffusion or any other flux leakage, its value remains constant, unlike M_J (for which

$$M_J \propto \frac{P^{3/2}}{\rho^2} \propto \rho^{3(\gamma-4/3)/2}$$

since $P \propto \rho^\gamma$ i.e., constant for $\gamma = 4/3$). M_{Φ_B} is around a third more than the observed mass except in the case of G2 for which the values are nearly the same. The characteristic magnetic mass (Bertoldi & McKee 1992):

$$M_B = 512\left(\frac{R}{Z}\right)^2 \frac{{B_{1.5}}^3}{{n_3}^2}$$

where

$$B_{1.5} = \frac{B}{10^{1.5}\mu\mathrm{G}} \text{ and } n_3 = \frac{n}{10^3}\ \mathrm{cm^{-3}},$$

is independent of core mass and does not vary much for the Coalsack cores, confirming its utility as "characteristic" of the Coalsack clump population; only collisions will greatly alter M_B. Once again for C2 this value is close to the observed value signifying its greater readiness to host a star-forming (e.g., $C^{18}O$) core within. The critical mass M_{CR} is that above which, accounting for thermal, turbulent, and magnetic pressures, the core becomes susceptible to gravitational collapse: $M_{\mathrm{CR}} = M_J + M_{\Phi_B}$, which is an approximate solution of M_{CR}'s governing equation (Mouschovias & Spitzer 1976):

$$M_{\mathrm{CR}} = 1.18\,M_J\left[1 - \left(\frac{M_{\Phi_B}}{M_J}\right)^2\right]^{-3/2}.$$

A.3. Column Density

To estimate the optical depth at the peak of the line, excitation temperature, and column density we used the same method as Vilas-Boas et al. (1994); namely four basic assumptions: (1) the product of beam efficiency and filling factor is the same for ^{13}CO as for C^{18}O, (2) the ^{13}CO and C^{18}O lines are formed in similar excitation conditions and the difference in the true value of the excitation temperatures T_{13} and T_{18} is less than the uncertainty in the deduced values due to the noise in the spectra, (3) in the observed regions the ^{13}CO and C^{18}O column density ratio is ∼5.5, the ratio of terrestrial abundances, and (4) in each cloud the observed ^{13}CO and C^{18}O lines are formed in regions with the same velocity gradient. Detailed discussion about these hypotheses is presented in Myers et al. (1983).

Using the definition of the absorption coefficient in LTE conditions, the ratio of optical depths is

$$\frac{\tau_{13}}{\tau_{18}} = \frac{[n_{13}(J=1)L_{13}\Delta V_{18} J(T_{18})]}{[n_{18}(J=1)L_{18}\Delta V_{13} J(T_{13})]},$$

where τ is the optical depth at the center of the line, ΔV is the line FWHM, L is the line-of-sight extent of the source, and

$$J(T) = \frac{T_0}{[e^{T_0/T} - 1]}$$

where

$$T_0 = \frac{h\nu}{\kappa},$$

ν is the transition frequency, and h and κ are Planck and Boltzmann's constants, respectively, with the subscripts specifying the isotopic variety. With this equation and the four assumptions above, $\tau_{13} = 5.5\tau_{18}$. Using assumption (1), the intensity ratio of both transitions obtained from the equation of radiative transfer in a homogenous medium is

$$\frac{T^*_{a13}}{T^*_{a18}} = \frac{[1 - \exp(-5.5\tau_{18})]}{[1 - \exp(-\tau_{18})]},$$

where T^*_a is the observed antenna temperature corrected for atmospheric opacity. This ratio is equal to the corresponding ratio of main-beam brightness temperatures allowing calculation of τ_{18}.

The excitation temperatures obtained from the solution of the radiative transfer equation are calculated with

$$\frac{T_0}{T_{18}} = \ln\left(1 + \frac{T_0}{J(T_{\rm bg}) + T^\star_{a18}/\eta_b\Phi(1 - \exp(-\tau_{18}))}\right),$$

where $T_{\rm bg} = 2.7$ K is the background radiation, η_b is the main beam efficiency, and Φ is the filling factor assumed to be one, as the emission regions are larger than the half-power beam width (33″). Assuming constant absorption throughout the cloud and a Gaussian shape for the observed lines, from the definition of optical depth:

$$N_{18} = \frac{8\pi\nu^2\kappa}{hc^3 A} U(T_{\rm ex}) \int T_a{}^* \, dV,$$

where $U(T_{\rm ex})$ is the classical partition function and ΔV is in km s^{-1}. The C^{18}O column density in the $J = 1$ level is

$$N_{18}(J=1) = 3.6 * 10^{14} \tau_{18} J(T_{18}) \Delta V_{18}\ {\rm cm}^{-2}.$$

This multiplied with the partition function ratio

$$\frac{\sum_{J=0}^{\rm max}(2J+1)\exp(-hBJ(J+1)/\kappa T_{18})}{3\exp(-2hB/\kappa T_{18})},$$

where B is the rotation constant for C^{18}O = 54.89 GHz, truncated at a $J_{\rm max}$ of seven, at which point the relative change in the sum is ⩽0.1%, gives the total column density. The C^{18}O lines are reasonably well fit with Gaussian profiles for all the cores so the uncertainty due to line shape is negligible in the above calculations applied to our observed lines.

REFERENCES

Andersson, B.-G., & Potter, S. B. 2005, MNRAS, 356, 1088
Andersson, B.-G., Wannier, P. G., & Crawford, I. A. 2002, MNRAS, 334, 327
Bertoldi, F., & McKee, C. F. 1992, ApJ, 395, 140
Bhat, N. D. R., & Andersson, B. 2011, ApJ, 729, 38
Brooks, J. W., Sinclair, M. W., & Manefield, G. A. 1976, MNRAS, 175, 117
Carolan, P. B., et al. 2009, MNRAS, 400, 78
Chandrasekhar, S., & Fermi, E. 1953, ApJ, 118, 116
Corradi, W. J. B., & Franco, G. A. P. 1995, A&AS, 112, 95
Evans, N. J., II. 1999, ARA&A, 37, 311
Franco, G. A. P. 1989, A&AS, 78, 105
Gómez, T., & Mendoza v, E. E. 1976, RevMexAA, 1, 381
Goodman, A. A., Benson, P. J., Fuller, G. A., & Myers, P. C. 1993, ApJ, 406, 528
Hara, A., Tachihara, K., Onishi, T., Mizuno, A., & Fukui, Y. 1999, in Star Formation 1999, ed. T. Nakamoto (Nagoya: Nobeyama Radio Observatory), 165
Hidajat, B. 1962, Contrib. Bosscha Obs., 16, 1
Jones, T. J., Hyland, A. R., & Bailey, J. 1984, ApJ, 282, 675
Jones, T. J., Hyland, A. R., Robinson, G., Smith, R., & Thomas, J. 1980, ApJ, 242, 132
Kato, S., Mizuno, N., Asayama, S.-i., Mizuno, A., Ogawa, H., & Fukui, Y. 1999, PASJ, 51, 883
Kenyon, S. J., & Hartmann, L. 1995, ApJS, 101, 117
Kerr, F. J., Hawarden, T. G., & Bowers, P. F. 1976, BAAS, 8, 335
Klessen, R. S., Heitsch, F., & Mac Low, M.-M. 2000, ApJ, 535, 887
Lada, C. J., Huard, T. L., Crews, L. J., & Alves, J. F. 2004, ApJ, 610, 303
Ladd, N., Purcell, C., Wong, T., & Robertson, S. 2005, PASA, 22, 62
Le Coarer, E., Amram, P., Boulesteix, J., Georgelin, Y. M., Georgelin, Y. P., Marcelin, M., Joulie, P., & Urios, J. 1992, A&A, 257, 389
McClure-Griffiths, N. M., Dickey, J. M., Gaensler, B. M., & Green, A. J. 2001, ApJ, 562, 424
Mouschovias, T. C., & Spitzer, L., Jr. 1976, ApJ, 210, 326
Muzzio, J. C., & Orsatti, A. M. 1977, AJ, 82, 345
Myers, P. C., Linke, R. A., & Benson, P. J. 1983, ApJ, 264, 517
Nakano, T. 1998, ApJ, 494, 587
Naoi, T., et al. 2007, ApJ, 658, 1114
Nyman, L.-A., Bronfman, L., & Thaddeus, P. 1989, A&A, 216, 185
Onishi, T., et al. 1999, PASJ, 51, 871
Otrupcek, R. E., & Wang, J.-S. 1987, PASA, 7, 194
Rathborne, J. M., Lada, C. J., Walsh, W., Saul, M., & Butner, H. M. 2009, ApJ, 690, 1659
Sault, R. J., Teuben, P. J., & Wright, M. C. H. 1995, in ASP Conf. Ser. 77, Astronomical Data Analysis Software and Systems IV, ed. R. A. Shaw, H. E. Payne, & J. J. E. Hayes (San Francisco, CA: ASP), 433
Savage, B. D., & Mathis, J. S. 1979, ARA&A, 17, 73
Seidensticker, K. J., & Schmidt-Kaler, T. 1989, A&A, 225, 192
Shu, F. H., Adams, F. C., & Lizano, S. 1987, ARA&A, 25, 23
Shu, F. H., & Li, Z. 1997, ApJ, 475, 251
Smith, R. G., Blum, R. D., Quinn, D. E., Sellgren, K., & Whittet, D. C. B. 2002, MNRAS, 330, 837
Smyth, M. J., & Sim, M. E. 1980, Nature, 283, 457
Tapia, S. 1973, in IAU Symp. 52, Interstellar Dust and Related Topics, ed. J. M. Greenberg & H. C. van de Hulst (Dordrecht: Reidel), 43
Tomisaka, K., Ikeuchi, S., & Nakamura, T. 1989, ApJ, 341, 220
Ungerechts, H., & Thaddeus, P. 1987, ApJS, 63, 645
Vilas-Boas, J. W. S., Myers, P. C., & Fuller, G. A. 1994, ApJ, 433, 96
Weaver, W. B. 1973, ApJ, 184, 881
Westerlund, B. E. 1961, Ark. Astron., 2, 429
Westerlund, B. E., & Garnier, R. 1989, A&AS, 78, 203
Wilking, B. A., Lada, C. J., & Young, E. T. 1989, ApJ, 340, 823